

# Design of a prototype split-and-delay unit for XFEL pulses, and their evaluation by synchrotron radiation X-rays

Jun'ya Sakamoto,<sup>a</sup> Kenji Ohwada,<sup>b,a\*</sup> Masahiko Ishino,<sup>c</sup> Jun'ichiro Mizuki,<sup>a</sup> Masami Ando<sup>d</sup> and Kazumichi Namikawa<sup>e</sup>

Received 5 July 2016

Accepted 7 November 2016

Edited by A. Momose, Tohoku University, Japan

**Keywords:** split-and-delay unit; Bragg case interferometer; XFEL; synchrotron radiation X-rays.

<sup>a</sup>School of Science and Technology, Kwasei Gakuin University, 2-1 Gakuen, Sanda, Hyogo 669-1337, Japan,

<sup>b</sup>Synchrotron Radiation Research Center (SPring-8), Kansai Photon Science Institute, Quantum Beam Science Research Directorate, National Institutes for Quantum and Radiological Science and Technology, 1-1-1 Kouto, Sayo, Hyogo 679-5148, Japan, <sup>c</sup>Department of Advanced Photon Research, Kansai Photon Science Institute, Quantum Beam Science Research Directorate, National Institutes for Quantum and Radiological Science and Technology, 8-1-7 Umemidai, Kizugawa, Kyoto 619-0215, Japan, <sup>d</sup>Tokyo University of Science, 6-3-1 Nijjuku, Katsushika-ku, Tokyo 125-8585, Japan, and <sup>e</sup>Tokyo Gakugei University, 4-1-1 Nukuikita-machi, Koganei, Tokyo 184-8501, Japan.

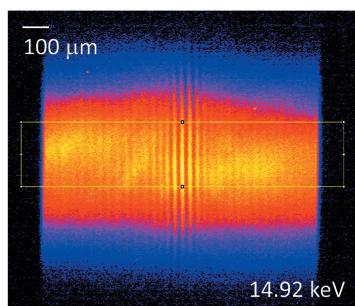
\*Correspondence e-mail: ohwada@spring8.or.jp

A prototype split-and-delay unit (SDU) for X-ray free-electron laser (XFEL) pulses is proposed based on the Graeff–Bonse four-Bragg-reflection interferometer by installing 12.5° slopes. The SDU can continuously provide a delay time from approximately –20 to 40 ps with a resolution of less than 26 fs. Because the SDU was constructed from a monolithic silicon crystal, alignment is straightforward. The obtained throughputs of the SDU reached 0.7% at 7.46 keV and 0.02% at 14.92 keV. The tunability of the delay time using the proposed SDU was demonstrated by finding the interference effects of the split X-rays, and the time resolution of the proposed SDU was evaluated using the width of the interference pattern recorded on the X-ray charge-coupled device camera by changing the energy, *i.e.* longitudinal coherence length, of the incident X-rays. It is expected that the proposed SDU will be applicable to XFEL experiments using delay times from tens of femtoseconds to tens of picoseconds, *e.g.* intensity correlation measurements.

## 1. Intensity correlation measurements for elucidating fluctuations in solids

The development of X-ray free-electron laser (XFEL) facilities in the hard X-ray regime, *e.g.* the Linac Coherent Light Source (LCLS) (Emma *et al.*, 2010) in the USA and the SPring-8 Angstrom Compact free-electron LAsER (SACLA) (Ishikawa *et al.*, 2012) in Japan, provides an avenue for experiments that have never been performed at third-generation synchrotron radiation facilities. Intensity correlation measurements and X-ray pump–probe measurements in the femtosecond to picosecond regions are leading examples; these techniques offer a powerful means of elucidating fluctuations in solids, which is of great interest in solid-state physics.

Intensity correlation measurements in the soft X-ray region have previously been realised using a single-shot highly brilliant plasma soft (13.9 nm) X-ray laser (Namikawa *et al.*, 2009; Ji *et al.*, 2009; Kishimoto *et al.*, 2010). Plasma-based soft X-ray lasers are characterized by pulse widths of several picoseconds, a spatial coherence of over 90% and  $\sim 10^{11}$  photons per pulse. A Michelson interferometer-type split-and-delay unit (SDU) was constructed using an X-ray beam splitter for soft X-rays and it successfully generated double-pulse



coherent X-rays with several picosecond delay times. These researchers employed a high-speed streak camera for the time-resolved measurement of the X-ray speckle patterns created by the double-pulse coherent X-rays. Intensity correlation measurements were performed to probe the relaxation phenomena of polarizations in polarization clusters in the paraelectric phase of the well known ferroelectrics BaTiO<sub>3</sub> near its Curie temperature ( $T_C \approx 400$  K).

The intensity correlation measurement can be widely applied to the relaxation phenomena of nanostructures in other solids, such as charge density waves in tetrathiafulvalene tetracyanoquinodimethane, spin density waves in anti-ferromagnetic chromium and stripes in cuprate high- $T_C$  superconductors. By using much shorter X-ray pulses, such as those produced by an XFEL, we can directly observe the relaxation process from the dynamical to the dissipative in the nanostructures of solids.

The SDU is a key component in intensity correlation measurements, which require *jitter-free* double pulses. Two SDUs are now operational in the extreme ultraviolet (XUV) and soft X-ray spectral regime at beamlines BL2 (Wöstmann *et al.*, 2013) and PG2 (Sorgenfrei *et al.*, 2010) at FLASH. The delay times, of the order of femtoseconds, were directly evaluated by interfering two time-delayed partial beams on a CCD camera (Mitzner *et al.*, 2008) and by time-resolved two-photon double ionization of He (Mitzner *et al.*, 2009). Several SDUs have been proposed for hard X-ray XFEL pulses: a Michelson interferometer-type SDU (Stetsko *et al.*, 2013), an SDU using the X-ray streaking method (David *et al.*, 2015), an SDU consisting of eight single crystals arranged in a 90° vertical-scattering geometry (Roseker *et al.*, 2009, 2011) and a wavelength-tunable split-and-delay optical system using a Bragg beam splitter combined with Kirkpatrick-Baez (KB) focusing mirrors (Osaka *et al.*, 2013, 2016).

Thus, SDUs based on different concepts are under development for operation in hard X-ray XFEL facilities. In this paper, we revisit a well established Bragg-case [Graeff–Bonse type (Graeff & Bonse, 1977; Fezzaa & Lee, 2001)] X-ray interferometer and propose a prototype SDU by making small changes to the interferometers. The presented SDU has advantages over the above-mentioned SDUs in terms of user-friendliness, delay-time-tunability and stability.

## 2. Design of a prototype split-and-delay unit

Fig. 1 shows a schematic of a Graeff–Bonse four-Bragg-reflection interferometer (Graeff & Bonse, 1977;

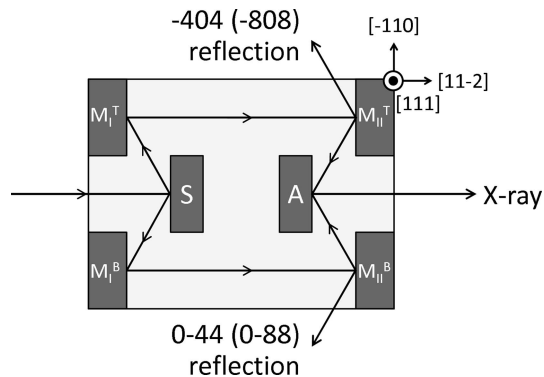


**Figure 1**  
Schematic of the Graeff–Bonse four-Bragg-reflection interferometer (Graeff & Bonse, 1977).

Fezzaa & Lee, 2001). The interferometer is constructed from a monolithic silicon crystal, with the structure shown in Fig. 1. An X-ray path along [112] is split into two paths by 404 and 044 simultaneous scattering at S; these paths then recombine at A after four bounces (S–M<sub>I</sub><sup>T,B</sup>–M<sub>II</sub><sup>T,B</sup>–A). The X-ray energy is confined by the {*hh*0} (for  $h = 2n$ ) plane indices. In the case of  $h = 4$  and 8 in Fig. 1, the X-ray energies are approximately 7.46 and 14.92 keV, respectively. These two indices will be used hereafter following Fezzaa & Lee (2001).

Fig. 2 shows the third-angle projection of the prototype SDU proposed in this paper. The present SDU should be symmetric about the B plane in Fig. 2. As shown in the cross-sectional drawing of C–C in Fig. 2, the M<sub>I</sub><sup>T</sup> and M<sub>II</sub><sup>T</sup> sections in

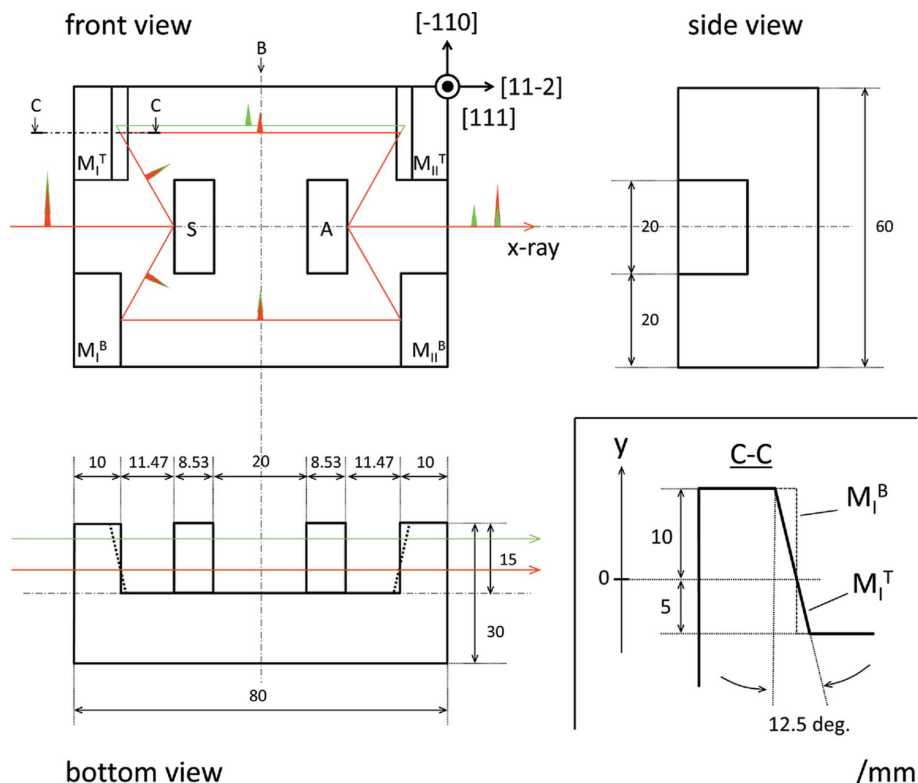


**Figure 2**  
Third-angle projection of the present SDU (dimension in millimetres).

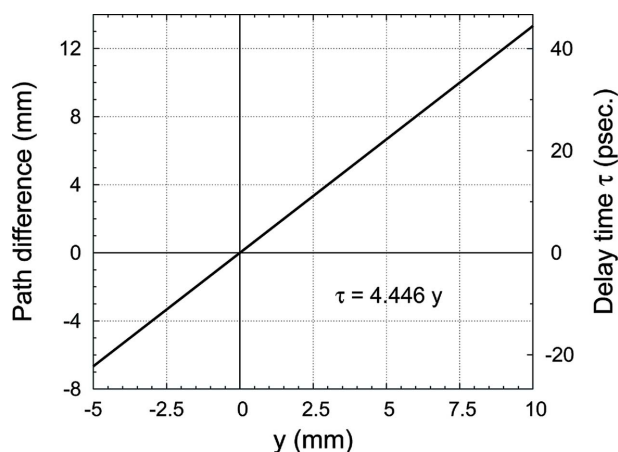


**Figure 3**  
Calculated delay time expected in the present SDU.

the SDU are cut with a  $12.5^\circ$  slope. This slope creates a delay time by changing the position of incidence ( $y$ -value in the cross-sectional drawing of C–C). Fig. 2 presents two examples: no delay time (red) and a finite delay time (green). The delay time is calculated as  $\tau$  (ps) =  $4.446 \times y$  (mm) on the basis of the dimensions shown in Fig. 2 and is displayed in Fig. 3. The present design has a linear range of approximately  $-20$  to  $40$  ps, where setting the range from negative to positive value will facilitate finding the exact zero delay time from the interference of the two split X-rays, and the jitter-free delay time is easily set by simply changing the position of the SDU, the  $y$ -value.

The actual prototype SDU was prepared by SUMTEC Service Corp. The crystal was carefully cut by end-milling, and the surfaces of S,  $M_I^{T,B}$ ,  $M_{II}^{T,B}$  and A were polished by #1200 carborundum and etched by more than  $50 \mu\text{m}$  to remove damaged and strained layers. Note that the conventional approach is to use the peripheral cutting edge instead of end-milling. However, the present process enabled the preparation

of the two types of surfaces  $M^T$  (with slope) and  $M^B$  (without slope) in one monolithic unit, as shown in the inset of Fig. 2. As is shown later, because the widths of the measured rocking curves are close to the calculated values, we concluded that the damaged and strained layers were almost completely removed. Some polishing flaws and surface roughness were also confirmed; however, they have a negligible effect on the present evaluation at SPring-8. These features should be removed before experiments at XFEL facilities, where an atomically flat surface (Osaka *et al.*, 2016) is required because of the spatially fully coherent X-rays.

### 3. X-ray evaluation of the prototype split-and-delay unit at SPring-8

The evaluation of the prototype SDU was performed at BL22XU (Shobu *et al.*, 2007) at SPring-8.

Fig. 4 shows a schematic of the experimental setup. X-rays from an in-vacuum undulator were monochromated by a liquid-nitrogen-cooled Si(111) double-crystal monochromator. The energy was tuned to approximately  $7.46 \text{ keV}$  ( $\lambda = 1.662 \text{ \AA}$ ) or  $14.92 \text{ keV}$  ( $\lambda = 0.831 \text{ \AA}$ ). As shown in Fig. 4, the monochromated X-rays were collimated by an upstream aperture to a certain size ( $200 \mu\text{m} \times 200 \mu\text{m}$  and  $1 \text{ mm} \times 1 \text{ mm}$ , in the present experiment) and then guided to the SDU. For the rocking curve measurements of  $hh0$  reflections, the centre of rotation was set at the edge and centre of S, as shown in Fig. 4. The outgoing X-rays from the SDU were recorded by a high-resolution X-ray charge-coupled device (CCD) camera (Ohwada *et al.*, 2007), where the effective pixel size was up to  $1.18 \mu\text{m} \times 1.18 \mu\text{m}$  and the number of pixels was  $4000$  (H)  $\times$   $2624$  (V). The image data were analyzed using *ImageJ* software (Abramoff *et al.*, 2004).

The performance was evaluated by the following scheme. (a) Show that the delay time can be precisely tuned by the SDU. Synchronize the two split pulses ( $\tau = 0$ ); an interference

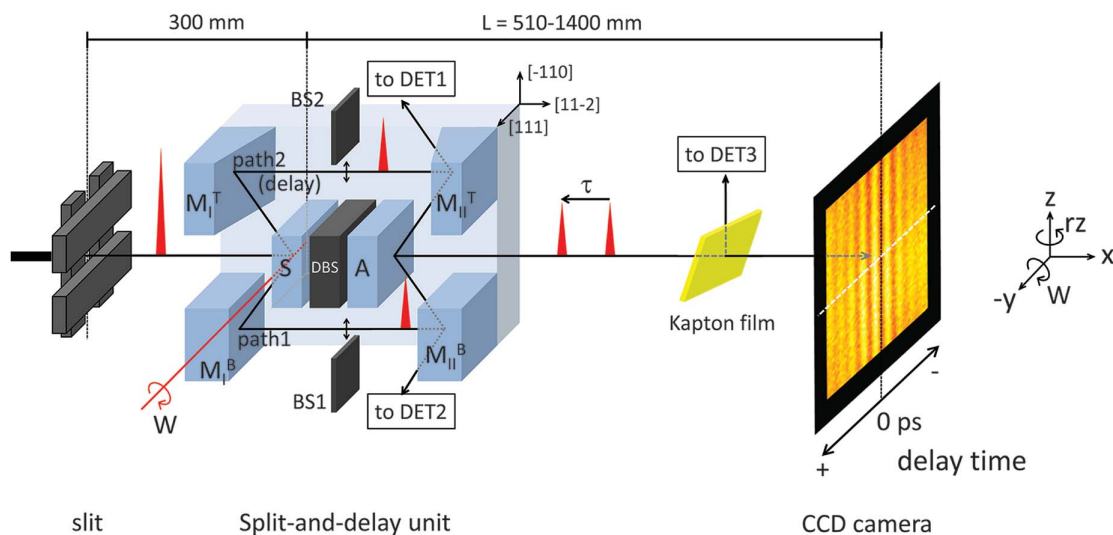


**Figure 4**  
Experimental setup for the evaluation of the prototype SDU at BL22XU. BS, DBS and DET denote beam stoppers, direct beam stoppers and detectors, respectively.

pattern should be observed by the high-resolution X-ray CCD camera. (b) Estimate the time resolution of the SDU on a femtosecond scale. The time resolution can be evaluated by the width of the interference pattern on the high-resolution CCD camera. Changing the incident X-ray energy (e.g. 7.46 to 14.92 keV) changes the longitudinal coherence length (e.g.  $\lambda^2/\Delta\lambda = 16.7$  to 80.0  $\mu\text{m}$ ) and thereby the width of the interference pattern on the high-resolution X-ray CCD camera.

### 3.1. Interference patterns: delay time = 0 ps

First, we tuned the energy of the incident X-rays such that simultaneous scattering occurs by monitoring the rocking curves using detectors 1 and 2 (DET1 and DET2). Fig. 5 shows the case of  $h = 4$  and 7.46 keV. The rocking curves detected by DET1 and DET2 are symmetric and isodynamic and approach each other as the energy is optimized to 7.46 keV ( $E_0$ ), as shown in Fig. 5. After the optimization, when simultaneous scattering occurred, the narrow profiles of the outgoing X-rays were observed by detector 3 (DET3), as also shown in Fig. 5.

The rocking curve widths observed by DET1 and DET2 well reflect the energy bandwidth of the incident X-rays from the Si(111) double-crystal monochromator. The rocking curve widths observed by DET1 and DET2 as shown in Fig. 5 are approximately  $0.007^\circ$  ( $= 25.2$  arcsec) and correspond to an energy bandwidth of 0.53 eV. On the other hand, the energy bandwidth of the 7.46 keV X-rays from Si(111) was calculated as 0.96 eV. The 0.43 eV difference can be explained by the detuning of the Si(111) double-crystal monochromator to avoid the higher-order reflection: the slight tilt of the second crystal of the monochromator (60% detune) narrows the energy bandwidth of the X-rays. This can be understood from the DuMond diagram mapping for two identical crystals arranged non-dispersively. If the trace of the second crystal slightly shifts (detuned) against that of the first crystal, the

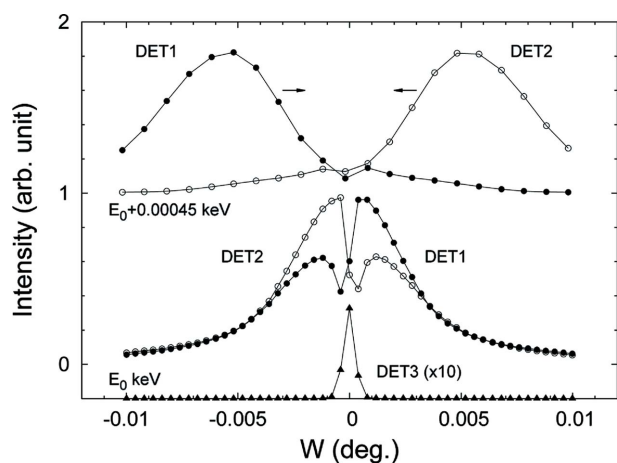


**Figure 5** Rocking curves measured by DET1, DET2 and DET3 as a function of incident energy by rotating the SDU. The two curves come close to each other and overlap just at  $E_0 = 7.46$  keV. We could observe clear output X-rays of the SDU by DET3 just at  $E_0$ .

resultant overlap region will determine the bandwidth of the outgoing X-rays to be narrower than that from the first crystal.

The throughput of the SDU, which is defined as the ratio of the intensities between SDU-in and SDU-out at DET3, were obtained as 0.4–0.7% for  $h = 4$ , 7.46 keV, and 0.01–0.02% for  $h = 8$ , 14.92 keV. The obtained values are approximately consistent with rough calculations based on the energy bandwidth and beam divergence of the incident X-rays and acceptance bandwidth, acceptance angle and absorption (four bounces) of the SDU as follows. In the case of  $h = 4$ , 7.46 keV, the bandwidth of the X-rays decreases to  $\sim 8\%$  by the acceptance bandwidth of the SDU, the beam divergence of the X-rays decreases to  $\sim 50\%$  by the acceptance angle of the SDU, the  $\sim 16\%$  X-rays are absorbed every bounce and half of X-rays go out of the optics after the third bounce (see Fig. 1), therefore the throughput of the SDU will be  $\sim 1\%$ . In the case of  $h = 8$ , 14.92 keV, the bandwidth of the X-rays decreases to  $\sim 0.8\%$ , the beam divergence of the X-rays decreases to  $\sim 10\%$ , the  $\sim 7\%$  X-rays are absorbed every bounce and so forth, therefore the throughput of the SDU will be  $\sim 0.03\%$ . In this paper, effects of the asymmetric diffraction narrowing the acceptance of the SDU by  $\sqrt{2}$  is not considered for simplicity.

Second, we used the high-resolution X-ray CCD camera to observe the interference pattern around the position of incidence,  $y = 0$ . The experimental conditions were as follows: (i)  $L = 510$  mm,  $E_i = 7.46$  keV ( $h = 4$ ), (ii)  $L = 1400$  mm,  $E_i = 7.46$  keV ( $h = 4$ ), (iii)  $L = 1400$  mm,  $E_i = 14.92$  keV ( $h = 8$ ) and (iv)  $L = 1000$  mm,  $E_i = 14.92$  keV ( $h = 8$ ), where  $L$  is the distance from the rotation center of the SDU to the CCD camera (see Fig. 4). Fig. 6(c) shows the interference stripes observed in the case of (i). The origin of the stripe pattern is discussed later.

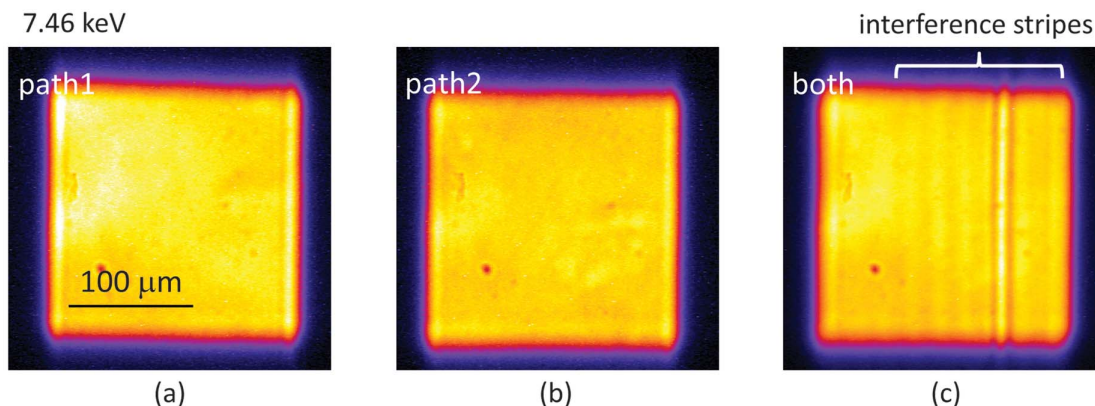
To verify the results, the X-rays from path 1 and path 2 were imaged, as shown in Fig. 6(a) and 6(b), respectively. The X-rays from path 1 (path 2) were imaged by inserting the beam stopper BS2 (BS1) in Fig. 4. The results show that the observed interference stripe patterns are certainly a result of the phase retardation/advancement of X-ray wave packets from the two paths.

The observation of the interference patterns demonstrates the successful finding of the position of zero delay time; therefore, the results indicate that this SDU can be used to easily and precisely tune the delay time by simply changing the position of incidence, the  $y$ -value.

Because the X-ray images from the two paths overlap well, we note that the SDU has actually been made approximately symmetric about the B plane in Fig. 2.

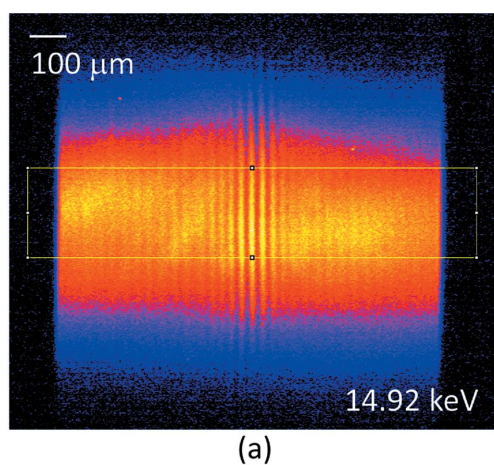
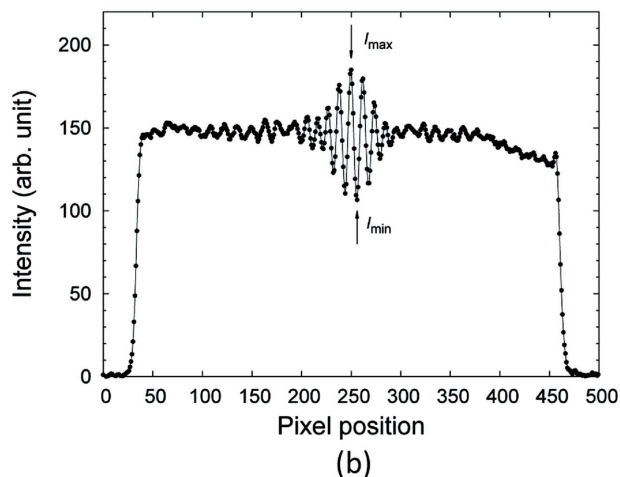
### 3.2. Evaluation of the delay time from the interference patterns

We obtained one-dimensional profiles from the interference patterns measured under the four experimental conditions (i)–(iv). Fig. 7(a) shows an image of the interference stripes in the case of (iii). The interference pattern is wider than that in the case of (i), shown in Fig. 6. The one-dimensional profile was obtained from Fig. 7(a) by integrating the vertical direction in


**Figure 6**

Images of the X-rays from (a) path 1, (b) path 2 and (c) both paths in the case of the experimental condition (i):  $L = 510$  mm,  $E_i = 7.46$  keV ( $h = 4$ ) measured by the high-resolution CCD camera (see Fig. 4). Interference stripes are clearly observed.

the box in Fig. 7(a), and the result is shown in Fig. 7(b). The fringes are clearly observed, and the visibility, defined by  $(I_{\max} - I_{\min}) / (I_{\max} + I_{\min})$ , is 0.269. The failure of the visibility to reach 1 is attributed to the partial coherence along the


**(a)**

**(b)**
**Figure 7**

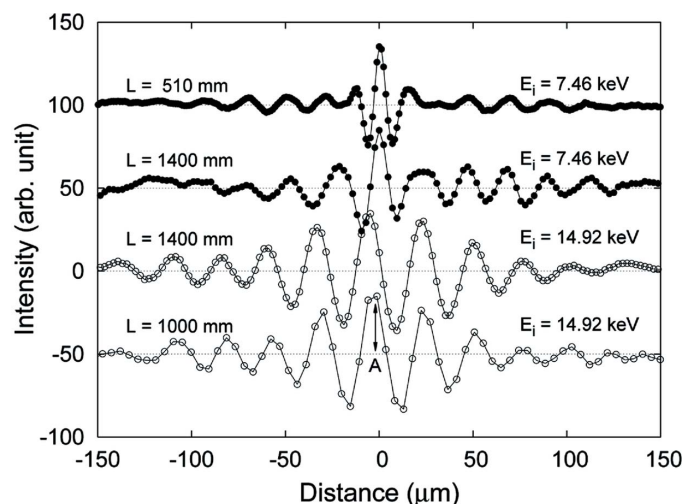
(a) Image of the interference stripes in the case of the experimental condition (iii)  $L = 1400$  mm,  $E_i = 14.92$  keV ( $h = 8$ ) measured by the high-resolution CCD camera (see Fig. 4). The interference pattern can be observed over a wider area than in the case of 7.46 keV ( $h = 4$ ) case. (b) The one-dimensional profile obtained from (a). The vertical direction in the box in (a) was integrated.

horizontal (the  $y$ -direction) of the SPring-8 X-rays and the instability of the incoming X-rays after the liquid-nitrogen-cooled Si(111) double-crystal monochromator of BL22XU.

Fig. 8 shows the one-dimensional profiles recorded for the four experimental conditions. The pixel positions of the X-ray CCD camera were converted to distances from the centre. One can notice that the period length of the amplitude is independent of the  $L$  parameter but dependent on the X-ray energy: as the X-ray energy increases, the length increases. This relationship is discussed later as an effect of the refraction of the X-rays.

The envelope curve of each profile is due to the effect of the longitudinal coherence lengths. As previously noted, changing the X-ray energy changes the longitudinal coherence length. In the present case, 7.46 and 14.92 keV X-rays have longitudinal coherence lengths of  $\lambda^2 / \Delta\lambda = 16.7$  and 80.0  $\mu\text{m}$ , respectively (only Darwin widths are considered). The longitudinal coherence length of 14.92 keV X-rays is approximately five times longer than that of 7.46 keV X-rays, as is immediately obvious from Fig. 8.

We focus on the amplitude ( $A$ ) of each profile shown in Fig. 8. Fig. 9 shows  $A^2$  as a function of the delay time. The


**Figure 8**

One-dimensional profiles for the four experimental conditions.

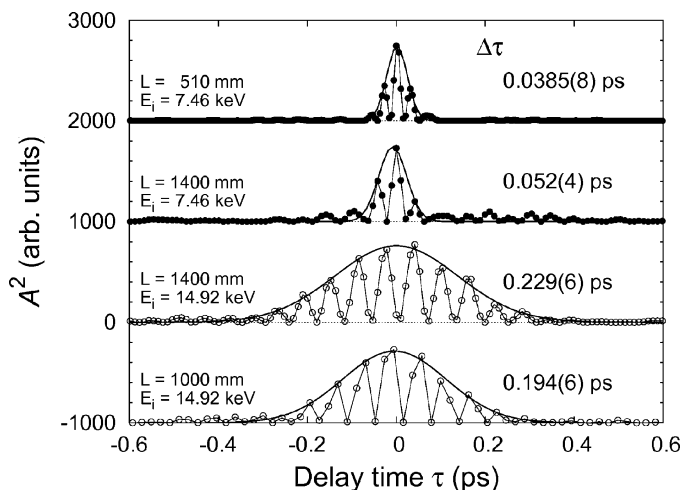


**Figure 9**  
 $A^2$  as a function of the delay time obtained from Fig. 8. The solid envelope curves are the double-Gaussian fitting results.

distance ( $\mu\text{m}$ ) in Fig. 8 is converted to the delay time (ps) using the relation shown in Fig. 3. The envelope curves are fitted by a double Gaussian as a function of the delay time  $x$ ,

$$g^2(x) = \left\{ a \exp \left[ -\frac{(x-b)^2}{2c^2} \right] \right\}^2, \quad (1)$$

where  $a$  is the amplitude,  $b$  is the centre ( $\sim 0$ ),  $c$  is the standard deviation and  $c\sqrt{2\ln 2}$  is the half width at half-maximum of  $g(x)$ , abbreviated hereafter as  $\Delta\tau_{\text{HWHM}}$ , the coherence time (Mitzner *et al.*, 2008). The fitting results are shown in Fig. 9 as solid lines. The calculated  $\Delta\tau_{\text{HWHM}}$  values are also shown:  $\Delta\tau_{\text{HWHM}} = 0.0385(8)$  to  $0.052(4)$  ps for 7.46 keV X-rays and  $0.194(6)$  to  $0.229(6)$  ps for 14.92 keV X-rays. Note that HWHM of  $g(x)$  corresponds to the half width at quarter-maximum of  $g^2(x)$  in Fig. 9.

We also checked the total accuracy of the systems. As the SDU moves along the  $y$ -axis ( $y_{\text{gonio}}$ ), the interference pattern will move into the viewing field of the X-ray CCD camera ( $y_{\text{CCD}}$ ). We obtained the relationship between  $y_{\text{gonio}}$  and  $y_{\text{CCD}}$  from the centre of mass of the interference pattern, as shown in Fig. 10. The gradient of the relationship was 1.006(1), showing that the total accuracy of the delay-time setting is within 0.6%.

## 4. Discussion

### 4.1. Delay time

The observed  $\Delta\tau_{\text{HWHM}}$  values are approximately similar to values estimated from the longitudinal coherence lengths of 0.056 and 0.267 ps for 7.46 and 14.92 keV, respectively. Furthermore,  $\Delta\tau_{\text{HWHM}}$  tends to increase as the length  $L$  increases. This increment trend could be at least partially due to the divergence of the scattered X-rays. In the case of  $L = 1400$  mm, we can compare  $\Delta\tau_{\text{HWHM}}$  directly. The ratio of the  $\Delta\tau_{\text{HWHM}}$  values for 7.46 and 14.92 keV is obtained from 1 to 4.4, which is similar to the calculated ratio from 1 to 4.8.

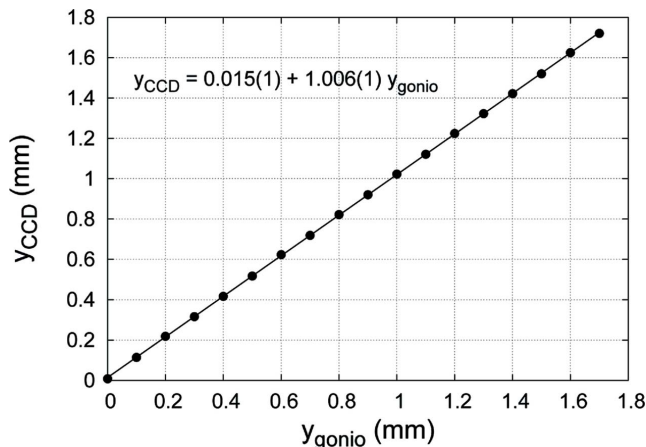


**Figure 10**  
 The relationship between  $y_{\text{gonio}}$  and  $y_{\text{CCD}}$  obtained on the basis of the centre of mass of the interference pattern.

As seen in Fig. 9, the time resolution of the SDU is clearly less than 77 fs; furthermore, three peaks are clearly separated in the case of  $E_i = 7.46$  keV, indicating that the time resolution of the SDU should be less than 26 fs. On the other hand, the present SDU might have an ambiguity of a few femtoseconds in the delay-time setting due to the processing accuracy of the present Si surfaces, which have been polished by #1200 carborundum and etched by more than  $50 \mu\text{m}$ , providing a surface roughness of less than  $10 \mu\text{m}$ . Because the pulse width of SACLA is reported as 6–30 fs (FWHM), the present time resolution will be sufficient for experiments with a delay time of over 30 fs on the condition that the beam size is negligibly small.

However, in practice, owing to the  $12.5^\circ$  slopes, the pulse width from path 2 ( $\Delta t_{p2}$  fs) strongly depends on the beam size ( $a \mu\text{m}$ ). Compared with the pulse width from path 1 ( $\Delta t_{p1}$  fs),  $\Delta t_{p2}$  will increase by  $4.446a$  fs. Because the beam size of SACLA is reported as  $\sim 80 \mu\text{m}$ ,  $\Delta t_{p2}$  will increase by  $\sim 356$  fs. For experiments with a femtosecond delay, such as investigation of electronic excitations, it will be necessary to narrow the X-ray beam, use a beam condenser to achieve a few-micrometres beam size along the  $y$ -direction before the SDU, or set a steeper slope angle in the SDU. The present SDU with  $12.5^\circ$  slopes is sufficient for investigating the lattice excitation ( $\sim$ ps).

The pointing, size and spectrum of XFEL pulses are not stable because of the self-amplified spontaneous emission process. The pointing and size stability of the XFEL pulses in SACLA are reported as approximately 10% and less than 5%, respectively (Lehmkühler *et al.*, 2015). These results indicate that the incident beam should be narrowed adequately by an aperture (for example, slit in Fig. 4). The instability of the spectrum will result in the shot-by-shot intensity fluctuation; however, it should be less serious for one-shot experiments using SDUs.

In the present case of  $h = 4$  and 8, as shown in Fig. 9, the longitudinal coherent lengths are longer than the width of the XFEL pulses, and the X-rays after the SDU will be highly coherent. Highly coherent X-rays are known to be highly

advantageous for intensity correlation measurements (Nami-kawa *et al.*, 2009).

#### 4.2. Origin of the interference stripes

We next discuss the origin of the interference stripes observed in Figs. 6(c) and 7. The period length of the amplitude is obtained as  $l_{\text{obs}} = 21.2 \mu\text{m}$  for 7.46 keV X-rays and  $28.3 \mu\text{m}$  for 14.92 keV X-rays. As mentioned previously, the period length of the amplitude is of the order of several tens of micrometres and is independent of the  $L$  parameter but not the X-ray energy: as the X-ray energy increases, the period length increases. These results clearly indicate that the interference stripes are not a result of a type of *double-slit* experiment.

We suppose that refraction contributes greatly to these interference stripes. Fig. 11 shows a schematic top-view drawing of the refraction that should occur at  $M_1^T$  and  $M_1^B$  in the present SDU. The optical path tilts very slightly (by  $\alpha^\circ$ ) owing to the  $12.5^\circ$  slope at the  $M_1^T$  section [see Fig. 11(a),  $\mathbf{k}_f^T$ ]; meanwhile, it does not tilt at the  $M_1^B$  section [see Fig. 11(b),  $\mathbf{k}_f^B$ ]. Fig. 11(c) shows a schematic drawing of the moiré pattern

created by the two waves  $\mathbf{k}_f^T$  and  $\mathbf{k}_f^B$ . Such a refraction occurs twice in this SDU during the four bounces.

By using the refraction indices,  $n = 0.99999116$  for 7.46 keV X-rays and  $n = 0.99999781$  for 14.92 keV X-rays, the  $\alpha$ -angles are calculated as  $0.00022479^\circ$  and  $0.00005585^\circ$ , respectively. Finally, the  $l$  values are calculated as  $l_c = 21.2 \mu\text{m}$  for 7.46 keV X-rays and  $42.7 \mu\text{m}$  for 14.92 keV X-rays.

The refraction-based model can easily explain the  $L$  independence of the period length of the amplitude. It also qualitatively explains the increasing tendency of the period length of the amplitude as the X-ray energy increases, as  $\delta$  of the refractive index  $n = 1 - \delta$  is inversely proportional to the square of the X-ray energy,  $E$ . The period length of the amplitude is quantitatively explained in the case of the 7.46 keV X-rays but not in the case of 14.92 keV X-rays. The origin of this mismatch is not yet understood.

Finally we describe how to resolve the two pulses with a femtosecond delay time. Because detectors with femtosecond-scale time resolutions do not yet exist, at least two approaches are considered. Both approaches use two-dimensional detectors, and the information of the two pulses is recorded in the same frame. The two images are superimposed on the CCD screen and then statistically separated after the experiments (Gutt *et al.*, 2009). The images are recorded separately on the same screen by inclining the two incident X-ray paths and crossing the two paths at the sample position (Roling *et al.*, 2014; David *et al.*, 2015). We are considering the latter case with a combination of focusing mirrors. Both approaches are elegant, but the strictly determined delay times are postulated. Because of its easy tuning of the delay time and its stability, we expect that the present SDU will be a powerful tool in forthcoming XFEL experiments.

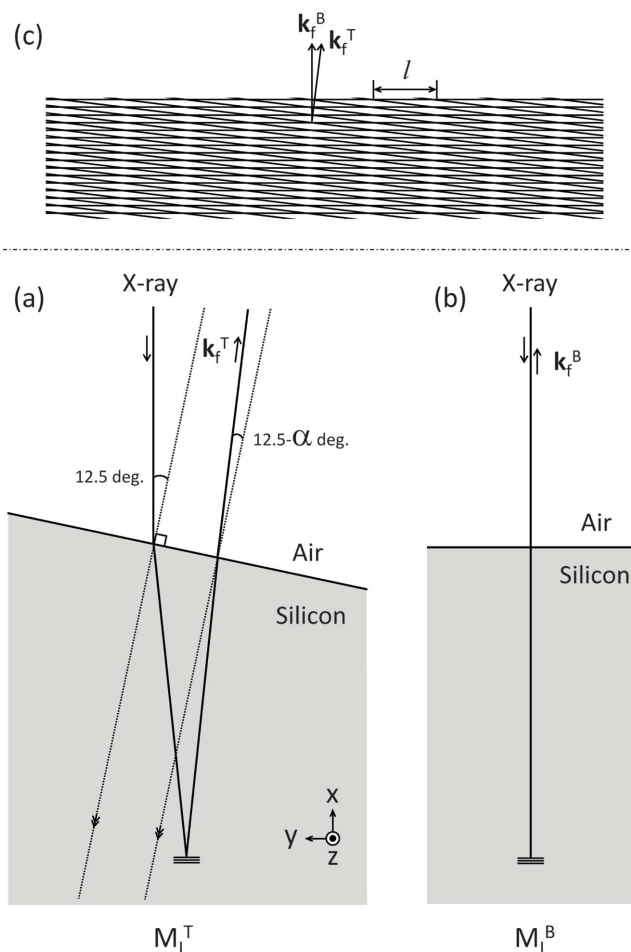


**Figure 11**  
Top-view schematic of the optical paths. Refraction occurs at (a)  $M_1^T$  but not (b)  $M_1^B$ . (c) A moiré pattern created by the two waves  $\mathbf{k}_f^T$  and  $\mathbf{k}_f^B$ .

#### 5. Summary

We have proposed a prototype SDU for XFEL pulses based on the Graeff–Bonse four-Bragg-reflection interferometer by installing  $12.5^\circ$  slopes. The SDU can continuously provide delay times from approximately  $-20$  to  $40$  ps with a resolution of less than  $26$  fs. Because the SDU was constructed from a monolithic silicon crystal, alignment is straightforward. The throughputs of the SDU reached  $0.7\%$  at  $7.46$  keV and  $0.02\%$  at  $14.92$  keV. The tunability of the delay time by the present SDU was demonstrated by finding the interference effects of the split X-rays, and the time resolution of the present SDU was evaluated by the width of the interference pattern recorded on the X-ray CCD camera by changing the energy, *i.e.* longitudinal coherence length, of the incident X-rays. We expect that the SDU proposed herein will be applicable to XFEL experiments using delay times from tens of femtoseconds to tens of picoseconds, *e.g.* intensity correlation measurements.

#### Acknowledgements

We would like to show our gratitude to the following people for the experiments, stimulating discussions and comments:

Dr M. Takahashi (QST), Mr T. Tazoe, Mr S. Masaki (SUMTEC Service Corporation), Dr T. Osaka, Dr M. Yabashi (RIKEN), Mr D. Shimizu and Mr A. Kida (Kwansei Gakuin University). This work was partly supported by RIKEN and Japan Atomic Energy Agency. The synchrotron radiation experiments were performed at BL22XU of SPring-8 with the approval of Japan Synchrotron Radiation Research Institute (JASRI) (Proposal Nos. 2014A3713 and 2014B3713).

## References

- Abramoff, M. D., Magelhaes, P. J. & Ram, S. J. (2004). *Biophoton. Int.* **11**, 36.
- David, C., Karvinen, P., Sikorski, M., Song, S., Vartiainen, I., Milne, C. J., Mozzanica, A., Kayser, Y., Diaz, A., Mohacsi, I., Carini, G. A., Herrmann, S., Färm, E., Ritala, M., Fritz, D. M. & Robert, A. (2015). *Sci. Rep.* **5**, 7644.
- Emma, P., Akre, R., Arthur, J., Bionta, R., Bostedt, C., Bozek, J., Brachmann, A., Bucksbaum, P., Coffee, R., Decker, F.-J., Ding, Y., Dowell, D., Edstrom, S., Fisher, A., Frisch, J., Gilevich, S., Hastings, J., Hays, G., Hering, P., Huang, Z., Iverson, R., Loos, H., Messerschmidt, M., Miahnahri, A., Moeller, S., Nuhn, H.-D., Pile, G., Ratner, D., Rzepiela, J., Schultz, D., Smith, T., Stefan, P., Tompkins, H., Turner, J., Welch, J., White, W., Wu, J., Yocky, G. & Galayda, J. (2010). *Nat. Photon.* **4**, 641–647.
- Fezzaa, K. & Lee, W.-K. (2001). *J. Appl. Cryst.* **34**, 166–171.
- Graeff, W. & Bonse, U. (1977). *Z. Phys. B*, **27**, 19–32.
- Gutt, C., Stadler, L.-M., Duri, A., Autenrieth, T., Leupold, O., Chushkin, Y. & Grübel, G. (2009). *Opt. Express*, **17**, 55–61.
- Ishikawa, T., Aoyagi, H., Asaka, T., Asano, Y., Azumi, N., Bizen, T., Ego, H., Fukami, K., Fukui, T., Furukawa, Y., Goto, S., Hanaki, H., Hara, T., Hasegawa, T., Hatsui, T., Higashiya, A., Hirono, T., Hosoda, N., Ishii, M., Inagaki, T., Inubushi, Y., Itoga, T., Joti, Y., Kago, M., Kameshima, T., Kimura, H., Kirihara, Y., Kiyomichi, A., Kobayashi, T., Kondo, C., Kudo, T., Maesaka, H., Maréchal, X. M., Masuda, T., Matsubara, S., Matsumoto, T., Matsushita, T., Matsui, S., Nagasono, M., Nariyama, N., Ohashi, H., Ohata, T., Ohshima, T., Ono, S., Otake, Y., Saji, C., Sakurai, T., Sato, T., Sawada, K., Seike, T., Shirasawa, K., Sugimoto, T., Suzuki, S., Takahashi, S., Takebe, H., Takeshita, K., Tamasaku, K., Tanaka, H., Tanaka, H., Tanaka, R., Togashi, T., Togawa, K., Tokuhisa, A., Tomizawa, H., Tono, K., Wu, S., Yabashi, M., Yamaga, M., Yamashita, A., Yanagida, K., Zhang, C., Shintake, T., Kitamura, H. & Kumagai, N. (2012). *Nat. Photon.* **6**, 540–544.
- Ji, K., Namikawa, K., Zheng, H. & Nasu, K. (2009). *Phys. Rev. B*, **79**, 144304.
- Kishimoto, M., Namikawa, K., Sukegawa, K., Yamatani, H., Hasegawa, N. & Tanaka, M. (2010). *Rev. Sci. Instrum.* **81**, 013905.
- Lehmkuhler, F., Kwaśniewski, P., Roseker, W., Fischer, B., Schroer, M. A., Tono, K., Katayama, T., Sprung, M., Sikorski, M., Song, S., Glowina, J., Chollet, M., Nelson, S., Robert, A., Gutt, C., Yabashi, M., Ishikawa, T. & Grübel, G. (2015). *Sci. Rep.* **5**, 17193.
- Mitzner, R., Siemer, B., Neeb, M., Noll, T., Siewert, F., Røling, S., Rutkowski, M., Sorokin, A., Richter, M., Juranic, P., Tiedtke, K., Feldhaus, J., Eberhardt, W. & Zacharias, H. (2008). *Opt. Express*, **16**, 19909–19919.
- Mitzner, R., Sorokin, A. A., Siemer, B., Røling, S., Rutkowski, M., Zacharias, H., Neeb, M., Noll, T., Siewert, F., Eberhardt, W., Richter, M., Juranic, P., Tiedtke, K. & Feldhaus, J. (2009). *Phys. Rev. A*, **80**, 025402.
- Namikawa, K., Kishimoto, M., Nasu, K., Matsushita, E., Tai, R. Z., Sukegawa, K., Yamatani, H., Hasegawa, H., Nishikino, M., Tanaka, M. & Nagashima, K. (2009). *Phys. Rev. Lett.* **103**, 197401.
- Ohwada, K., Namikawa, K., Mizuki, J., Shimomura, S., Nakao, H., Ito, K., Matsushita, M., Yoneda, Y., Murakami, Y. & Hirota, K. (2007). *Trans. Mater. Res. Soc. Jpn.* **32**, 7.
- Osaka, T., Hirano, T., Sano, Y., Inubushi, Y., Matsuyama, S., Tono, K., Ishikawa, T., Yamauchi, K. & Yabashi, M. (2016). *Opt. Express*, **24**, 9187–9201.
- Osaka, T., Yabashi, M., Sano, Y., Tono, K., Inubushi, Y., Sato, T., Ogawa, K., Matsuyama, S., Ishikawa, T. & Yamauchi, K. (2013). *Proc. SPIE*, **8848**, 884804.
- Røling, S., Zacharias, H., Samoylova, L., Sinn, H., Tschentscher, T., Chubar, O., Buzmakov, A., Schneidmiller, E., Yurkov, M. V., Siewert, F., Braun, S. & Gawlitza, P. (2014). *Phys. Rev. ST Accel. Beams*, **17**, 110705.
- Roseker, W., Franz, H., Schulte-Schrepping, H., Ehnes, A., Leupold, O., Zontone, F., Lee, S., Robert, A. & Grübel, G. (2011). *J. Synchrotron Rad.* **18**, 481–491.
- Roseker, W., Franz, H., Schulte-Schrepping, H., Ehnes, A., Leupold, O., Zontone, F., Robert, A. & Grübel, G. (2009). *Opt. Lett.* **34**, 1768–1770.
- Shobu, T., Tozawa, K., Shiwaku, H., Konishi, H., Inami, T., Harami, T. & Mizuki, J. (2007). *AIP Conf. Proc.* **879**, 902–906.
- Sorgenfrei, F., Schlotter, W. F., Beeck, T., Nagasono, M., Gieschen, S., Meyer, H., Föhlisch, A., Beye, M. & Wurth, W. (2010). *Rev. Sci. Instrum.* **81**, 043107.
- Stetsko, Y. P., Shvyd'ko, Y. V. & Brian Stephenson, G. (2013). *Appl. Phys. Lett.* **103**, 173508.
- Wöstmann, M., Mitzner, R., Noll, T., Røling, S., Siemer, B., Siewert, F., Eppenhoff, S., Wahlert, F. & Zacharias, H. (2013). *J. Phys. B*, **46**, 164005.